A homogeneous thermal-to-mechanical time-scale ratio and its near-wall behavior

I. Otić

Karlsruhe Institute of Technology (KIT), Hermann-von-Helmholtz-Platz 1, 76344 Eggenstein-Leopoldshafen, Germany

ivan.otic@kit.edu

July 20, 2026

Abstract. The dissipation rate ε_θ of the temperature variance, and the thermal-to-mechanical time-scale ratio formed from it, vary sharply across the near-wall layer in most flows. Using the two-point correlation method, ε_θ is split into a homogeneous part $\varepsilon_{\theta,h}$ and an inhomogeneous part that is absorbed exactly by the molecular diffusion in the transport equation of $\overline{\theta^2}$. The variance transport equation then retains $\varepsilon_{\theta,h}$ as its dissipation and defines a homogeneous time-scale ratio $\mathcal{R}_h = \overline{\theta^2}\,\varepsilon_h/(2k\,\varepsilon_{\theta,h})$, where ε_h is the homogeneous dissipation rate of the turbulent kinetic energy k. Expressed through the mechanical and thermal Taylor microscales, λ and λ_θ, the ratio becomes $\mathcal{R}_h = (5/C_\theta)\,Pr\,(\lambda_\theta/\lambda)^2$. At an isothermal wall both microscales are linear in the wall distance, so $\mathcal{R}_h$ is smooth and approaches the molecular limit $\mathcal{R}_h|_w = Pr$ monotonically; at Prandtl numbers of order one its near-wall variation is reduced relative to the classical time-scale ratio R, which departs from and returns to the same wall value. The two ratios are related by the exact factorization $R = \mathcal{R}_h(1 - f_\theta)/(1 - f_u)$, in which the inhomogeneous fractions of the two dissipations, $f_\theta = \varepsilon_{\theta,ih}/\varepsilon_\theta$ and $f_u = \varepsilon_{ih}/\varepsilon$, carry the entire difference between them and equal one half at the wall. The factorization locates the crossing of R through its wall value just outside the sign change of the mechanical fraction, at $y^+ \simeq$ 6–8 over the Prandtl-number range studied. At walls with fluctuating temperature, constant-flux, Robin or conjugate, both ratios are singular, diverging as $\overline{\theta^2}_w\,(y^+)^{-2}$ with an amplitude fixed by wall values. The analysis is assessed against channel-flow direct numerical simulation databases from three independent codes, at $Pr = 0.71$, 0.025 and 0.01 and under isothermal, constant-flux, Robin and conjugate thermal conditions. The data confirm the isothermal wall limit, the monotone approach, the location of the crossing, and the singular asymptote with its analytical amplitude. In a wall-anchored a priori reconstruction of ε_θ with no adjustable constant, the constant-$\mathcal{R}_h$ closure is exact through the conductive sublayer and its error is one-signed, while the error of the classical constant-R closure changes sign at the crossing. Being exact, the analysis provides a physical basis for the constant time-scale ratio of turbulent heat-flux models and a constraint for data-driven closures.

1 Introduction

The transport equation for the temperature variance $\overline{\theta^2}$ has been central to scalar-turbulence theory since Corrsin [1]. A key quantity is the thermal-to-mechanical time-scale ratio

$$R \;\equiv\; \frac{\overline{\theta^2}/(2\varepsilon_\theta)}{k/\varepsilon} \;=\; \frac{\overline{\theta^2}\,\varepsilon}{2k\,\varepsilon_\theta}, \tag{1}$$

formed from the mechanical time scale $\tau_u = k/\varepsilon$ and the thermal time scale $\tau_\theta = \overline{\theta^2}/(2\varepsilon_\theta)$; here $\overline{\theta^2}$ is the temperature variance, ε_θ its dissipation rate, k the turbulent kinetic energy and ε its dissipation rate. Algebraic and second-moment heat-flux closures approximate ε_θ through a prescribed value of R (see e.g. Launder [2], Newman *et al.* [3], Hanjalić [4]). The ratio is not a universal constant: equal power-law decay of k and $\overline{\theta^2}$ would make R constant, but the decay exponents differ (see e.g. Corrsin [1], Lumley and Newman [5], Warhaft and Lumley [6], Warhaft [7]), and R depends on Reynolds number and on the scalar forcing [8, 9]. A near-constant R is observed only in restricted homogeneous conditions, such as behind a heated grid (see e.g. Lin and Lin [10]). All of these results concern a passive scalar. In the buoyancy-influenced or driven flows the temperature is dynamically active: the buoyancy production $\beta g_i\,\overline{u_i\theta}$, with β the thermal expansion coefficient and g_i gravity, couples the heat flux to the momentum field, and the thermal time scale $\tau_\theta = \overline{\theta^2}/(2\varepsilon_\theta)$ sets the rate at which buoyancy induces turbulence production. A deficiency in the approximation of ε_θ, equivalently in the time-scale ratio, then feeds back on the velocity field, so that its consequences are more severe than the approximation error of the passive case, see e.g. Otić *et al.* [11].

For the kinetic-energy dissipation, Kolovandin and Vatutin [12] and Jovanović *et al.* [13] showed, by the two-point correlation technique first introduced by Chou [14] and Burgers [15], that ε separates into a homogeneous part ε_h and an inhomogeneous part confined to the wall vicinity. Jakirlić and Hanjalić [16] used this technique to model the stress dissipation with the correct near-wall asymptotics, and Jakirlić and Jovanović [17] used the linear near-wall variation of the Taylor microscale, $\varepsilon_h = 5\nu q^2/\lambda^2$ with $\lambda \sim y$, to construct wall boundary conditions that relax the near-wall grid requirement.

Here the technique is applied to the temperature variance dissipation rate and to the time-scale ratio. The decomposition of ε_θ in §2.1 is their scalar analogue, which removes the inhomogeneity of ε_θ exactly. The main contributions are (i) the homogeneous time-scale ratio $\mathcal{R}_h$, which is introduced in §2.2 and requires no further assumptions, (ii) the exact variance equation formed with it, and (iii) the near-wall behavior of both ratios, derived analytically for isothermal walls and for walls with fluctuating temperature, constant-flux, Robin or conjugate (§3). In support of (iii), the exact factorization $R = \mathcal{R}_h(1-f_\theta)/(1-f_u)$ of the classical ratio is introduced, with f_θ and f_u the inhomogeneous fractions of the two dissipations: an immediate consequence of the definitions that explains the crossing of R through its wall value in the wall vicinity. The analytical results are then assessed in §4 against channel-flow direct numerical simulation (DNS) databases from three independent codes: the finite-difference simulations of Abe *et al.* [18] at $Pr = 0.71$ and 0.025, the incompact3d simulations of Flageul *et al.* [19] at $Pr = 0.71$ under Dirichlet, Neumann, Robin and conjugate thermal conditions, and the pseudo-spectral liquid-sodium simulations of Tiselj and Cizelj [20] at $Pr = 0.01$. The assessment confirms the wall limits and identifies a viscous-scaled crossing of R through its wall value at $y^+ \simeq 6$–8, common to all Prandtl numbers and located by the factorization. These results are shown to explain, and to indicate how to improve, the constant time-scale ratio used in turbulent heat-flux models, with a perspective for data-driven closures (§5). Finally, a summary is provided in §6.

2 The homogeneous time-scale ratio

2.1 Decomposition of the dissipation rate

With the Reynolds decomposition $U_i = \overline{U_i} + u_i$, $T = \overline{T} + \theta$, where $\overline{(\cdot)}$ is an ensemble average, the exact transport equation for $\overline{\theta^2}$ is

$$\frac{\mathrm{D}\overline{\theta^2}}{\mathrm{D}t} = -\frac{\partial}{\partial x_j}\,\overline{u_j\theta^2} - 2\,\overline{u_j\theta}\,\frac{\partial \overline{T}}{\partial x_j} + 2\kappa\,\overline{\theta\,\frac{\partial^2\theta}{\partial x_j \partial x_j}}, \tag{2}$$

with material derivative $\mathrm{D}/\mathrm{D}t = \partial_t + \overline{U}_j\,\partial/\partial x_j$ and κ the thermal diffusivity. Writing $\partial_j \equiv \partial/\partial x_j$ and $\partial_{jj} \equiv \partial_j\partial_j$, the molecular term is rewritten exactly through the identity $2\theta\,\partial_{jj}\theta = \partial_{jj}\theta^2 -$

$2\,\partial_j\theta\,\partial_j\theta$,

$$2\kappa\,\theta\,\overline{\frac{\partial^2\theta}{\partial x_j\partial x_j}} = \underbrace{\kappa\,\Delta_x\overline{\theta^2}}_{\text{molecular diffusion}} \quad -2\,\underbrace{\kappa\,\overline{\partial_j\theta\,\partial_j\theta}}_{\varepsilon_\theta}, \tag{3}$$

with $\Delta_x \equiv \partial^2/\partial x_j\partial x_j$, giving

$$\frac{\mathrm{D}\overline{\theta^2}}{\mathrm{D}t} = \underbrace{-\frac{\partial}{\partial x_j}\overline{u_j\theta^2}}_{D_\theta^t} + \underbrace{\kappa\,\Delta_x\overline{\theta^2}}_{D_\theta^m} \underbrace{-\,2\,\overline{u_j\theta}\,\frac{\partial\overline{T}}{\partial x_j}}_{P_\theta} -2\varepsilon_\theta, \tag{4}$$

where $\varepsilon_\theta = \kappa\,\overline{\partial_j\theta\,\partial_j\theta} \geq 0$ is the scalar dissipation rate and D_θ^t, D_θ^m, P_θ are the turbulent diffusion, molecular diffusion and production, respectively. The production P_θ contains the turbulent heat flux $\overline{u_j\theta}$, which is supplied by the accompanying algebraic or second-moment heat-flux closure. Apart from the triple correlation D_θ^t, which is not treated here and we refer to Deardorff [21], Hanjalić and Launder [22] or Otić *et al.* [11], the only remaining term requiring closure is ε_θ.

Following Chou [14], Burgers [15] (see also Hinze [23]), the fluctuating scalar is referred to two points A, B through the relative and centroid coordinates

$$\xi_k = (x_k)_B - (x_k)_A, \qquad (x_k)_{AB} = \tfrac{1}{2}[(x_k)_A + (x_k)_B]\,, \tag{5}$$

so that, with $\partial_{\xi_k} \equiv \partial/\partial\xi_k$ and $(\partial_k)_{AB} \equiv \partial/\partial(x_k)_{AB}$, the single-point derivatives are $(\partial_k)_A = \frac{1}{2}(\partial_k)_{AB} - \partial_{\xi_k}$ and $(\partial_k)_B = \frac{1}{2}(\partial_k)_{AB} + \partial_{\xi_k}$, whence, with summation over the repeated index k and $(\partial_k^2)_{AB} \equiv (\partial_k)_{AB}(\partial_k)_{AB}$,

$$(\partial_k)_A(\partial_k)_B = \tfrac{1}{4}\,(\partial_k^2)_{AB} - \partial_{\xi_k}^2. \tag{6}$$

Kinematic relations of this multi-point type, and their role in the nonlocality of turbulence, are analyzed by Kholmyansky and Tsinober [24] and Kholmyansky *et al.* [25]. Applying (6) to $\overline{(\theta)_A(\theta)_B}$ and taking the limit $\xi \to 0$, in which $\overline{(\theta)_A(\theta)_B} \to \overline{\theta^2}$ and $(\partial_k^2)_{AB} \to \Delta_x$, gives the identity

$$\frac{\varepsilon_\theta}{\kappa} = \overline{\partial_k\theta\,\partial_k\theta} = \tfrac{1}{4}\,\Delta_x\overline{\theta^2} \;-\; \big(\Delta_\xi\,\overline{\theta\theta'}\big)_0, \tag{7}$$

with $\Delta_\xi \equiv \partial^2/\partial\xi_k\partial\xi_k$, where the prime denotes the value at B and the subscript 0 the limit $\xi \to 0$. In a homogeneous field the two-point correlation is maximal at coincidence, so $(\Delta_\xi\overline{\theta\theta'})_0 \leq 0$ there. In an inhomogeneous field neither contribution in (7) is sign-definite on its own. We define

$$\varepsilon_\theta = \varepsilon_{\theta,h} + \varepsilon_{\theta,ih}, \quad \varepsilon_{\theta,h} \equiv -\kappa\big(\Delta_\xi\overline{\theta\theta'}\big)_0, \quad \varepsilon_{\theta,ih} \equiv \tfrac{1}{4}\kappa\,\Delta_x\overline{\theta^2}, \tag{8}$$

the homogeneous part $\varepsilon_{\theta,h}$ being the curvature of the two-point correlation and the inhomogeneous part $\varepsilon_{\theta,ih}$ a function of the mean variance field. In a homogeneous field $\Delta_x\overline{\theta^2} = 0$ and $\varepsilon_\theta = \varepsilon_{\theta,h}$. The inhomogeneous part is proportional to the Laplacian of the variance field and changes sign at inflection points of the $\overline{\theta^2}$ profile. At the wall $\Delta_x\overline{\theta^2}|_w > 0$, so both parts are positive there, as used in §3. The DNS profiles of §4 show $\varepsilon_{\theta,h} > 0$ at every point of every case considered. The inhomogeneous part $\varepsilon_{\theta,ih}$ contributes mainly in the wall layer and vanishes away from it, persisting further into the channel at lower Prandtl number owing to the larger thermal diffusivity (figure 1); its sign changes coincide with the inflection points of the variance profile.

Substituting $\varepsilon_\theta = \varepsilon_{\theta,h} + \frac{1}{4}\kappa\Delta_x\overline{\theta^2}$ into the transport equation (4) yields

$$\frac{\mathrm{D}\overline{\theta^2}}{\mathrm{D}t} = -\frac{\partial}{\partial x_j}\overline{u_j\theta^2} + \tfrac{1}{2}\kappa\,\Delta_x\overline{\theta^2} - 2\,\overline{u_j\theta}\,\frac{\partial\overline{T}}{\partial x_j} - 2\,\varepsilon_{\theta,h}\;. \tag{9}$$

The inhomogeneous part has been absorbed exactly by the molecular diffusion $\kappa\Delta_x\overline{\theta^2}$, so that the remaining dissipation term requiring a model is the homogeneous $\varepsilon_{\theta,h}$.

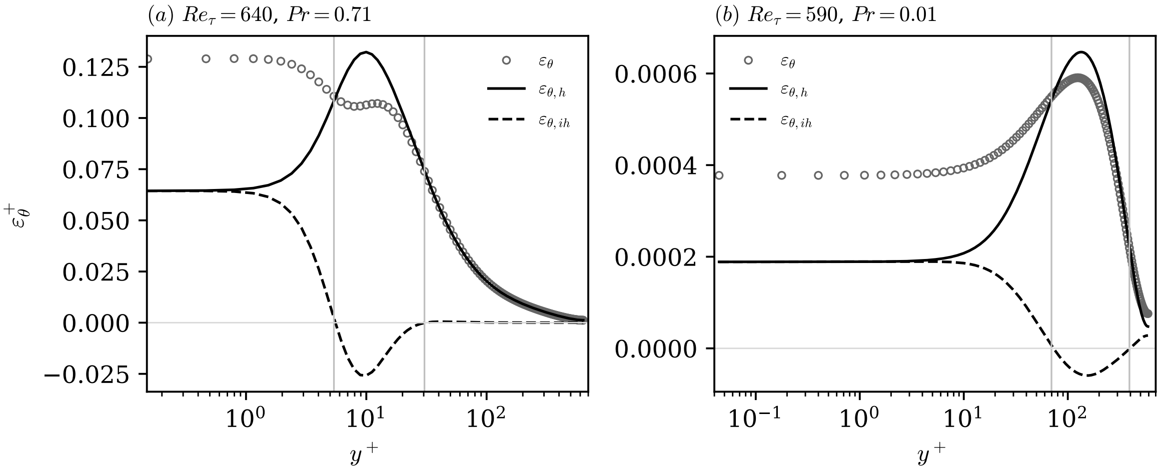

Figure 1: Decomposition (8) at isothermal channel walls: (a) $Re_\tau = 640$, $Pr = 0.71$, DNS data [18]; (b) $Re_\tau = 590$, $Pr = 0.01$, non-fluctuating thermal condition, DNS data [20]. ε_θ ($\circ$), $\varepsilon_{\theta,h}$ (solid), $\varepsilon_{\theta,ih}$ (dashed). Vertical lines mark the sign changes of $\varepsilon_{\theta,ih}$ at the inflection points of the variance profile, at $y^+ \approx 5.4$ and 30.4 in (a) and moving outward to $y^+ \approx 70$ in (b). In (a) the profiles are shown over the resolved range of the database, whose first grid point is at $y^+ \approx 0.2$; the data in (b) include the wall point, at which $\varepsilon_{\theta,h}|_w = \varepsilon_{\theta,ih}|_w = \frac{1}{2}\varepsilon_\theta|_w$ holds exactly, confirming (21). At the lower Prandtl number the inhomogeneous part persists far into the channel.

The kinetic-energy dissipation obeys the analogous relation [12, 13], with ν the kinematic viscosity. Applying (6) to $\overline{(u_i)_A(u_i)_B}$, where $\overline{(u_i)_A(u_i)_B} \to \overline{u_i u_i} = 2k$, gives

$$\varepsilon = \varepsilon_h + \varepsilon_{ih}, \qquad \varepsilon_h \equiv -\nu\big(\Delta_\xi \overline{u_i u_i'}\big)_0, \qquad \varepsilon_{ih} \equiv \tfrac{1}{2}\nu\,\Delta_x k, \tag{10}$$

in which the prime again denotes the value at B. The sign properties are those of (8): neither part is sign-definite in an inhomogeneous field, while at the wall $\Delta_x k|_w > 0$ and both parts are positive, as shown in §3.

2.2 Definition and Taylor-microscale form

In parallel with (1) we form the homogeneous-field time scales $\tau_{u,h} = k/\varepsilon_h$ and $\tau_{\theta,h} = \overline{\theta^2}/(2\varepsilon_{\theta,h})$ and define the homogeneous time-scale ratio

$$\mathcal{R}_h \equiv \frac{\tau_{\theta,h}}{\tau_{u,h}} = \frac{\overline{\theta^2}\,\varepsilon_h}{2k\,\varepsilon_{\theta,h}} \tag{11}$$

which inserted into (9) gives the exact transport equation

$$\frac{\mathrm{D}\overline{\theta^2}}{\mathrm{D}t} = -\frac{\partial}{\partial x_j}\overline{u_j\theta^2} + \tfrac{1}{2}\kappa\,\Delta_x\overline{\theta^2} - 2\,\overline{u_j\theta}\,\frac{\partial \overline{T}}{\partial x_j} - \frac{1}{\mathcal{R}_h}\,\frac{\varepsilon_h}{k}\,\overline{\theta^2}. \tag{12}$$

Equation (12) is an identity equivalent to (9). Its purpose is to focus the modeled content of the variance dissipation in the single dimensionless field $\mathcal{R}_h$, defined from homogeneous-field quantities, for which a velocity field model (k, ε_h) is available in a two-equation or second-moment closure.

The homogeneous dissipations (7) and (10) are the curvatures of the two-point correlations at the origin, that is, inverse-square Taylor microscales. For the velocity field this relation originates in the microscale definition of Taylor [26] (see also Tennekes and Lumley [27]) and is used in the near-wall context by Jakirlić and Jovanović [17],

$$\varepsilon_h = 5\nu\,\frac{q^2}{\lambda^2} = 10\nu\,\frac{k}{\lambda^2}, \qquad q^2 = \overline{u_i u_i} = 2k, \tag{13}$$

which defines the mechanical Taylor microscale λ. The thermal Taylor microscale λ_θ is defined analogously through the homogeneous scalar dissipation,

$$\varepsilon_{\theta,h} = C_\theta\,\kappa\,\frac{\overline{\theta^2}}{\lambda_\theta^2}, \tag{14}$$

where C_θ is a locally homogeneous coefficient. $C_\theta = 3$ when λ_θ is referred to one scalar-gradient component, though its value cancels in the wall limit, as shown below. The homogeneous time scales are then $\tau_{u,h} = \lambda^2/(10\nu)$ and $\tau_{\theta,h} = \lambda_\theta^2/(2C_\theta\kappa)$, so that (11) reduces to

$$\mathcal{R}_h = \frac{\lambda_\theta^2/(2C_\theta\kappa)}{\lambda^2/(10\nu)} = \frac{5}{C_\theta}\,Pr\left(\frac{\lambda_\theta}{\lambda}\right)^2, \qquad Pr \equiv \frac{\nu}{\kappa}. \tag{15}$$

In homogeneous isotropic turbulence $\varepsilon_\theta = \varepsilon_{\theta,h}$ and $\varepsilon = \varepsilon_h$, and (15) coincides with the microscale form of the passive-scalar time-scale ratio given by Ristorcelli [8]. His equation (11), $r = \frac{3}{5}\,Sc^{-1}(\lambda/\lambda_\theta)^2$ with Sc the Schmidt number, is the inverse of (15) ($r = 1/R$, mechanical-to-thermal), and his scalar dissipation $\varepsilon_c = 3D\langle c^2\rangle/\lambda_c^2$, here $\varepsilon_{\theta,h} = 3\kappa\overline{\theta^2}/\lambda_\theta^2$, sets the constant at $C_\theta = 3$ based on the homogeneous isotropic turbulence theory. The new element here is that the homogeneous time scale ratio (11) based on the decomposition (8) makes (15) the microscale ratio of the *homogeneous part* of the dissipation, so that it carries over to the wall layer with no model required for the inhomogeneity and without assuming the local isotropy that fails near the wall. The normalization constants 5 and C_θ of the two microscales cancel in the wall limit, as shown below.

The homogeneous time-scale ratio is therefore, up to a constant, the Prandtl number times the squared ratio of the thermal to the mechanical Taylor microscale. As a ratio of two microscales, $\mathcal{R}_h$ is better conditioned near the wall than R, which retains the steep near-wall structure of the full dissipations ε_θ and ε through their inhomogeneous parts; this is demonstrated on DNS data in §4 (figure 2).

The relation between the two ratios is exact. With the inhomogeneous fractions

$$f_u \equiv \frac{\varepsilon_{ih}}{\varepsilon}, \qquad f_\theta \equiv \frac{\varepsilon_{\theta,ih}}{\varepsilon_\theta}, \tag{16}$$

the definitions (1) and (11) give

$$R \;=\; \mathcal{R}_h\,\frac{1-f_\theta}{1-f_u}. \tag{17}$$

Equation (17) is an immediate algebraic consequence of the definitions; its value lies in what it organizes. The two ratios differ only through the inhomogeneous fractions, the sign of $R - \mathcal{R}_h$ is the sign of $f_u - f_\theta$, and the near-wall crossing of R through its wall value is located by (17) in §4.2.

3 Near-wall behavior

3.1 Velocity field

Let $y \equiv x_3$ be the wall-normal coordinate, the subscript w denote evaluation at the wall ($y \to 0$), and the fluctuations be expanded as

$$u_i = a_i + b_i y + c_i y^2 + \cdots, \qquad \theta = a_\theta + b_\theta y + \gamma_\theta y^2 + \cdots, \tag{18}$$

the coefficients $a_i, b_i, c_i, a_\theta, b_\theta, \gamma_\theta$ being fluctuating fields on (x_1, x_2, t). No slip gives $a_i = 0$ over the entire wall plane, continuity $\partial_i u_i = 0$ forces $\partial_3 u_3|_w = 0$, hence $b_3 = 0$. Thus $u_1 = b_1 y$, $u_2 = b_2 y$, $u_3 = c_3 y^2$ to leading order, and

$$\begin{aligned} k &= \tfrac{1}{2}\,\overline{(b_1^2 + b_2^2)}\, y^2 + O(y^4), \qquad \varepsilon|_w = \nu\,\overline{(b_1^2 + b_2^2)}, \\ \varepsilon_{ih}|_w &= \tfrac{1}{2}\nu\,\Delta_x k|_w = \tfrac{1}{2}\varepsilon|_w, \end{aligned} \tag{19}$$

so that $\varepsilon_h|_w = \varepsilon|_w - \varepsilon_{ih}|_w = \frac{1}{2}\varepsilon|_w$ and, from (13),

$$\lambda^2 = \left.\frac{10\nu k}{\varepsilon_h}\right|_w = \frac{10\nu\,\frac{1}{2}\overline{(b_1^2 + b_2^2)}\, y^2}{\frac{1}{2}\nu\,\overline{(b_1^2 + b_2^2)}} = 10\, y^2, \quad \lambda = \sqrt{10}\, y, \tag{20}$$

recovering the linear near-wall variation of the microscale used by Jakirlić and Jovanović [17]. These results are independent of the thermal wall condition and the derivation is provided for completeness. Note also, for use below, that (19) gives the leading-order $k = \frac{1}{2}(\varepsilon|_w/\nu)\, y^2$.

3.2 Isothermal wall

A fixed wall temperature gives $\theta|_w = 0$, hence $a_\theta = 0$, the fluctuating wall heat flux being carried by $b_\theta \neq 0$. Then $\theta = b_\theta y + O(y^2)$ and

$$\begin{aligned} \overline{\theta^2} &= \overline{b_\theta^2}\, y^2 + O(y^3), \qquad \varepsilon_\theta|_w = \kappa\,\overline{b_\theta^2}, \\ \varepsilon_{\theta,ih}|_w &= \tfrac{1}{4}\kappa\,\Delta_x \overline{\theta^2}|_w = \tfrac{1}{2}\varepsilon_\theta|_w, \end{aligned} \tag{21}$$

so that $\varepsilon_{\theta,h}|_w = \frac{1}{2}\varepsilon_\theta|_w$, and from (14)

$$\lambda_\theta^2 = \left.\frac{C_\theta \kappa\,\overline{\theta^2}}{\varepsilon_{\theta,h}}\right|_w = \frac{C_\theta \kappa\,\overline{b_\theta^2}\, y^2}{\frac{1}{2}\kappa\,\overline{b_\theta^2}} = 2C_\theta\, y^2, \quad \lambda_\theta = \sqrt{2C_\theta}\, y. \tag{22}$$

Both microscales are linear in y, so $(\lambda_\theta/\lambda)^2|_w = C_\theta/5$ and (15) gives

$$\mathcal{R}_h\big|_w = \frac{5}{C_\theta}\, Pr \cdot \frac{C_\theta}{5} = Pr\,. \tag{23}$$

The constant C_θ cancels, so the limit is independent of the microscale normalization. The total ratio R has the same limit: substituting (19) and (21) into (1) gives $R|_w = \nu/\kappa = Pr$, the molecular wall value established for the scalar time scale in wall turbulence [16]. The distinction between $\mathcal{R}_h$ and R is therefore not the wall value but the approach to it: by (15), $\mathcal{R}_h$ is set by the ratio of two near-linear microscales and remains close to Pr through the conductive layer, whereas R retains the inhomogeneous parts $\varepsilon_{\theta,ih}$ and ε_{ih}, which peak in the buffer and conductive layers and make R depart from Pr before returning to it. The wall identities $\varepsilon_{\theta,h}|_w = \varepsilon_{\theta,ih}|_w = \frac{1}{2}\varepsilon_\theta|_w$ and $\varepsilon_h|_w = \varepsilon_{ih}|_w = \frac{1}{2}\varepsilon|_w$ require the two ratios to coincide at $y = 0$. In terms of (17), both inhomogeneous fractions equal one half at the wall, $f_u|_w = f_\theta|_w = \frac{1}{2}$, and the condition for R to cross its wall value, $R = Pr$, takes the exact form

$$(\mathcal{R}_h - Pr)\,(1 - f_\theta) \;=\; Pr\,(f_\theta - f_u), \tag{24}$$

a balance between the departure of $\mathcal{R}_h$ from its anchor and the imbalance of the inhomogeneous fractions. The near-wall behavior of the variance dissipation in the buoyancy-driven case, in which the temperature is dynamically active, was analyzed for isothermal walls in the Rayleigh–Bénard DNS of Otić *et al.* [11]; the behavior of both ratios is quantified on channel-flow DNS in §4.2.

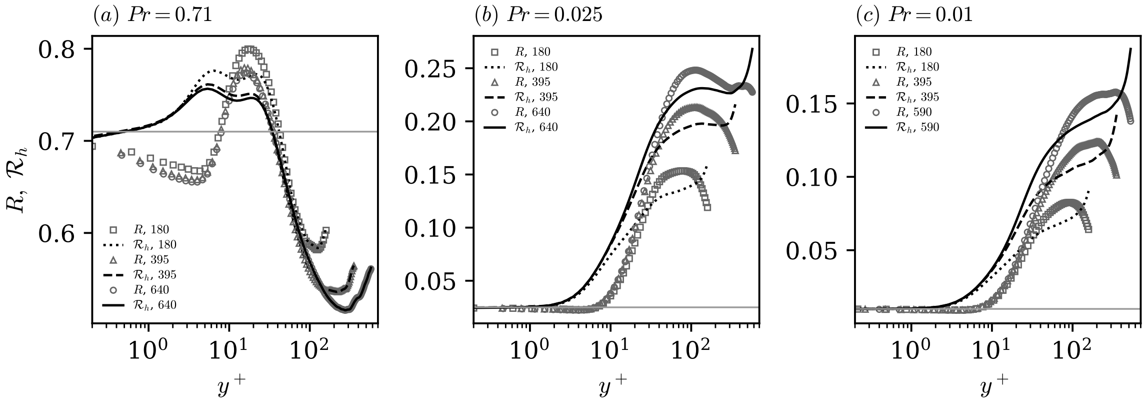

Figure 2: R (symbols) and $\mathcal{R}_h$ (lines) at isothermal walls: (*a*) $Pr = 0.71$ and (*b*) $Pr = 0.025$, $Re_\tau = 180, 395, 640$, DNS data [18]; (*c*) $Pr = 0.01$, $Re_\tau = 180, 395, 590$, non-fluctuating thermal condition, DNS data [20]. Horizontal lines mark the analytical wall limit Pr. Profiles are shown for $y^+ \leq 0.9\, Re_\tau$; nearer the centerline both homogeneous dissipations are small and their ratio is statistically noisy.

3.3 Constant-flux wall

A fixed wall heat flux (the constant-flux condition, also referred to as the isoflux or Neumann condition) gives $\partial_3\theta|_w = 0$, hence $b_\theta = 0$, while the wall temperature fluctuates, $a_\theta \neq 0$. Then $\theta = a_\theta + \gamma_\theta y^2 + \cdots$ and, with $\nabla_\parallel \equiv (\partial/\partial x_1, \partial/\partial x_2)$ the wall-parallel gradient,

$$\overline{\theta^2}\big|_w = \overline{a_\theta^2} \neq 0, \qquad \varepsilon_\theta\big|_w = \kappa\, \overline{|\nabla_\parallel a_\theta|^2} \neq 0, \tag{25}$$

the dissipation now being set by the wall-parallel gradients of the fluctuating wall temperature rather than by a wall-normal gradient. The variance does not vanish at the wall, so the thermal microscale tends to a finite, non-zero value, $\lambda_\theta^2|_w = C_\theta \kappa\, \overline{a_\theta^2}/\varepsilon_{\theta,h}|_w = O(1)$, whereas $\lambda = \sqrt{10}\, y \to 0$. Hence (15) gives

$$\mathcal{R}_h,\, R \;\sim\; Pr\, \frac{\overline{a_\theta^2}}{\overline{|\nabla_\parallel a_\theta|^2}}\, \frac{1}{y^2} \;\xrightarrow{y\to 0}\; \infty. \tag{26}$$

The time-scale ratio is singular at a constant-flux wall, and the decomposition does not remove the singularity because it originates in $\lambda_\theta \not\to 0$ rather than in the dissipation. The leading-order amplitude of the divergence follows from the wall expansions with no adjustable constant: inserting $k = \frac{1}{2}(\varepsilon|_w/\nu)\, y^2$ and the wall values of the dissipations into (1) and (11) gives, in wall units,

$$R \to \frac{\overline{\theta^2}_w}{\varepsilon_\theta|_w}\, (y^+)^{-2}, \qquad \mathcal{R}_h \to \frac{\overline{\theta^2}_w}{2\, \varepsilon_{\theta,h}|_w}\, (y^+)^{-2}, \tag{27}$$

where the mechanical identity $\varepsilon_h|_w = \frac{1}{2}\varepsilon|_w$, which holds regardless of the thermal condition, resolves the factor two. The Pr wall limit (23) is thus specific to the isothermal wall.

More generally, (27) shows that the singularity is present whenever the wall variance $\overline{\theta^2}_w$ is finite, at Neumann, Robin and conjugate walls, with an amplitude proportional to $\overline{\theta^2}_w$. For the isothermal (Dirichlet) wall, $\overline{\theta^2}_w = 0$. Flageul *et al.* [19] derived, for non-conjugate thermal conditions, the analytical relation between the thermal boundary condition, the wall variance and the wall-normal part of ε_θ, and Flageul *et al.* [28] analyzed the discontinuity of ε_θ at a conjugate interface. Those results concern the wall values of ε_θ and its wall-normal part. The decomposition (8), the ratio $\mathcal{R}_h$ built from its homogeneous part, and the limits (23) and (27) do not appear in their analysis, which we use below as an independent cross-check. The singularity

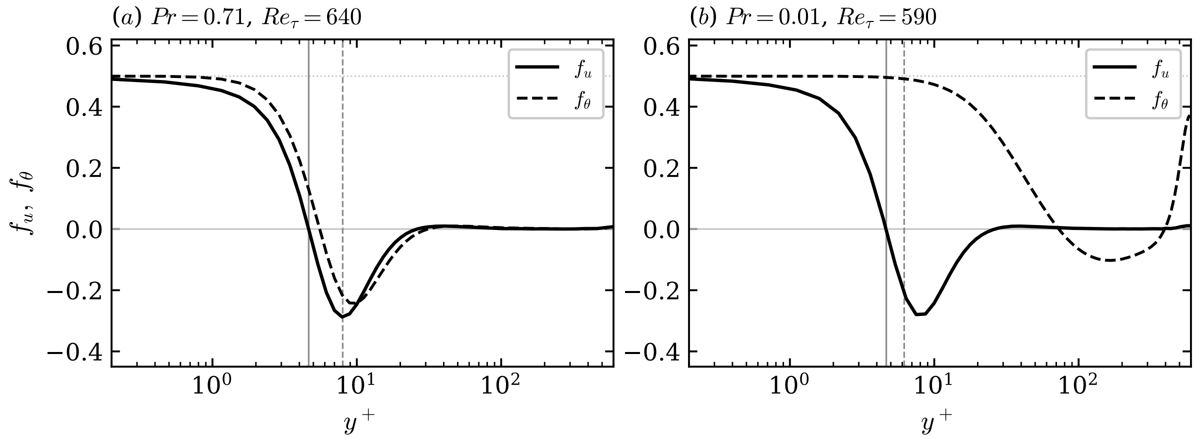

Figure 3: Inhomogeneous fractions (16) at isothermal walls: f_u (solid) and f_θ (dashed) for (a) $Pr = 0.71$, $Re_\tau = 640$, DNS data [18] and (b) $Pr = 0.01$, $Re_\tau = 590$, DNS data [20]; both fractions are evaluated from the tabulated budget terms. Both fractions start from the wall value $\frac{1}{2}$ (dotted line). The vertical solid line marks the sign change of ε_{ih} at the inflection point of k ($y^+ = 4.64$ and 4.65), the vertical dashed line the crossing $R = Pr$ of the balance (24) ($y^+ \approx 7.98$ and 6.19). The mechanical fraction is nearly identical in the two panels, while the thermal fraction retains its wall value through the thick conductive layer at low Pr.

is a property of the physical configuration, not a defect of $\mathcal{R}_h$, and R shares it; it is demonstrated on DNS data, together with the amplitude in (27), in §4.3. The constant-flux result delimits the analysis and is directly relevant to heated-wall configurations discussed in §5. For Robin and conjugate walls the linear term $b_\theta y$ re-enters the expansion and contributes $\kappa\,\overline{b_\theta^2}$ to $\varepsilon_\theta|_w$, without altering (27), which involves only the wall values.

4 Assessment against channel-flow DNS

4.1 Databases and conventions

Three published channel-flow DNS databases from independent codes are used. (i) The finite-difference simulations of Abe, Kawamura and co-workers [18, 29, 30] at $Re_\tau = 180$, 395 and 640 with $Pr = 0.71$ and 0.025. The thermal forcing is a uniform mean heat flux with zero wall-temperature fluctuation, the mixed-type condition of Kasagi *et al.* [31]; the condition seen by the fluctuating field is therefore Dirichlet, and every case realizes the isothermal wall of §3.2. This classification is confirmed directly from the data: the variance decays quadratically, $\overline{\theta^2} \sim y^2$, at both Prandtl numbers and all Reynolds numbers. (ii) The simulations of Flageul *et al.* [19] with the sixth-order compact-finite-difference code incompact3d at $Re_\tau \simeq 150$, $Pr = 0.71$, with tabulated variance budgets for four thermal conditions: Dirichlet, Neumann (imposed flux), Robin and three-dimensional conjugate. (iii) The pseudo-spectral simulations of Tiselj and Cizelj [20] at $Pr = 0.01$ (liquid sodium), $Re_\tau = 180$, 395 and 590, with two ideal thermal conditions per Reynolds number (non-fluctuating, i.e. isothermal for the fluctuation, and fluctuating, i.e. imposed flux) including full budgets, and a conjugate sweep of wall thickness d^+ and thermal activity ratio $K = \sqrt{\rho_f c_{pf} \lambda_f / (\rho_w c_{pw} \lambda_w)}$ for which wall-variance profiles are available.

In all datasets $\varepsilon_{\theta,ih} = \frac{1}{4}\kappa \Delta_x \overline{\theta^2}$ and $\varepsilon_{ih} = \frac{1}{2}\nu \Delta_x k$ are evaluated from the tabulated molecular-diffusion budget terms, and normalization conventions are fixed by the wall identities of §3 rather than assumed: at the Dirichlet walls the computed ratios $\varepsilon_{ih}/\varepsilon|_w$ and $\varepsilon_{\theta,ih}/\varepsilon_\theta|_w$ equal the analytical value $\frac{1}{2}$ to within 0.6% in every case (0.500 to three decimal places in the spectral data, which store the wall point). Budget-closure residuals are below 2.6% of the peak dissipation

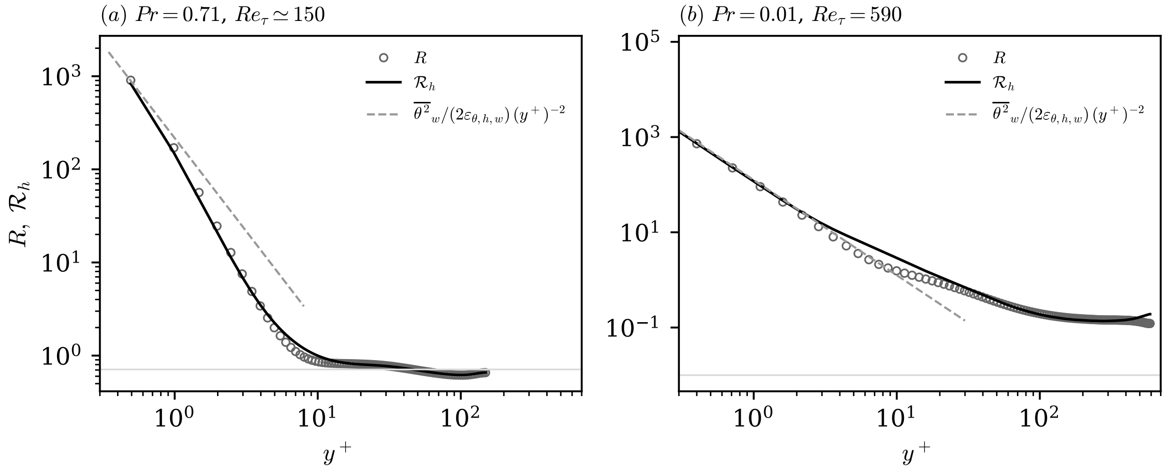

Figure 4: Constant-flux (Neumann) walls: R ($\circ$), $\mathcal{R}_h$ (solid) and the parameter-free asymptote (27) (dashed). (a) $Pr = 0.71$, $Re_\tau \simeq 150$, DNS data [19]; (b) $Pr = 0.01$, $Re_\tau = 590$, DNS data [20]. The -2 slope is the $y^+ \to 0$ limit; at $Pr = 0.71$ the finite-y^+ slope is steeper because ε_θ still varies across the thin conductive layer.

throughout. Wall values quoted below as extrapolations refer to quadratic fits over the first grid points ($y^+ < 1.5$), with relative fit residuals below 0.2%. Both ratios are evaluated on the native grid of each database; symbols and lines in the figures distinguish R from $\mathcal{R}_h$, not different data sources. At the Neumann wall of Tiselj and Cizelj [20] and Flageul *et al.* [19] the wall-normal part of $\varepsilon_\theta|_w$ vanishes identically, confirming that the dissipation there is carried by the wall-parallel gradients of the fluctuating wall temperature, as in (25).

4.2 Isothermal walls

Figure 2 shows R and $\mathcal{R}_h$ for the isothermal series at the three Prandtl numbers. The wall limit (23) is recovered in every case: extrapolation of the finite-difference data [18, 29, 30] gives $\mathcal{R}_h|_w$ within 1.5–2.8% of Pr, and the spectral data at $Pr = 0.01$ give $\mathcal{R}_h|_w = Pr$ to 0.1% at all three Reynolds numbers. The approach to the wall differs between the two ratios exactly as the analysis predicts. $\mathcal{R}_h$ approaches Pr monotonically in all ten isothermal cases. R departs from Pr and returns to it, crossing its own wall value once, at $y^+ = 6.1$–8.0. This crossing scales in viscous units and is nearly independent of Pr, although the thermal inhomogeneous part extends far beyond the buffer layer at low Pr (figure 1b). The factorization (17) locates it. The mechanical fraction f_u is a property of the velocity field alone: it falls from its wall value $\frac{1}{2}$, changes sign at the inflection point of the k profile, at $y^+ = 4.6$–5.1 in all ten cases and all three codes, and reaches its negative extremum in the buffer layer (figure 3). The crossing condition (24) then places $R = Pr$ just outside this sign change in both Prandtl regimes, for different reasons. At $Pr = 0.71$ both fractions are negative at the crossing ($f_u \simeq -0.28$, $f_\theta \simeq -0.17$ to -0.22) and $\mathcal{R}_h$ exceeds its anchor by only 6–9% there. At the low Prandtl numbers f_θ remains near its wall value $\frac{1}{2}$ through the thick conductive layer (figure 3b), but the imbalance term in (24) carries the prefactor Pr and is therefore weak, so the balance is reached where $\mathcal{R}_h$ has risen to 2.2–2.4 Pr, again immediately outside the mechanical sign change, with $f_u \simeq -0.16$ to -0.23 at the crossing, a departure invisible on the absolute scale of figure 2(c) yet exceeding a factor of two relative to the small anchor, so that the monotone approach at low Pr is not slow in relative terms. In all ten cases the crossing of R is thus tied to the negative excursion of ε_{ih} that begins at the Pr-independent inflection point of k, which explains the viscous scaling. At $Pr = 0.71$ the total variation of $\mathcal{R}_h$ over $y^+ < 30$ is half that of R (0.055–0.073 versus 0.118–0.133) and

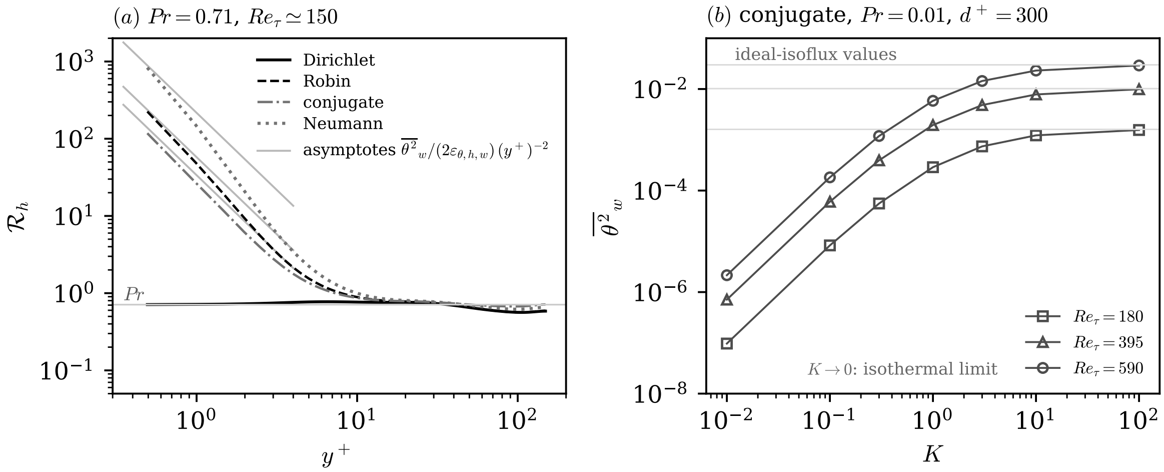

Figure 5: (a) $\mathcal{R}_h$ for the four thermal conditions of Flageul *et al.* [19] at $Pr = 0.71$: the Dirichlet wall is regular and anchored at Pr; Robin, conjugate and Neumann walls are singular with amplitudes ordered by the wall variance. Thin gray lines are the parameter-free asymptotes (27) of the three singular members, with amplitudes $\overline{\theta^2}_w/(2\varepsilon_{\theta,h}|_w) = 57.7$ (Robin), 33.7 (conjugate) and 216.5 (Neumann). (b) Wall variance $\overline{\theta^2}_w$ of the conjugate wall versus thermal activity ratio K at wall thickness $d^+ = 300$ [20]: the conjugate wall interpolates over four decades between the ideal-isoflux plateau ($K \gg 1$, horizontal lines) and the isothermal limit ($K \to 0$).

the near-wall $\mathcal{R}_h$ profiles collapse across $Re_\tau = 180$–640. At the lower Prandtl numbers both ratios are smooth; R remains close to Pr through the thick conductive layer, up to $y^+ \approx 8$, while $\mathcal{R}_h$ departs earlier because $\varepsilon_{\theta,ih}$ penetrates further at low Pr, and the near-wall variation grows with Reynolds number, consistent with the Reynolds-number dependence of near-wall temperature statistics at low Pr reported by Tiselj and Cizelj [20]. The near-wall $\mathcal{R}_h$ of the two independent codes at $Pr = 0.71$ agrees to better than 0.02 at matched y^+ between $Re_\tau \simeq 150$ [19] and $Re_\tau = 180$ [18]. These statements are established for forced channel flow at $Pr \le 0.71$ and $Re_\tau \le 640$; their extension to $Pr > 1$ and to buoyancy-driven flows remains to be examined.

4.3 Walls with fluctuating temperature: the $(y^+)^{-2}$ asymptote and its amplitude

The isothermal condition of §4.2 is distinguished by a fluctuation-free wall temperature. Every other thermal condition, constant-flux, Robin or conjugate, admits a finite wall variance $\overline{\theta^2}_w$, and both ratios are then singular, diverging as $\overline{\theta^2}_w\,(y^+)^{-2}$ because the variance remains finite at a wall where the kinetic energy vanishes quadratically. The asymptote (27) is parameter-free. Its exponent and its amplitude are fixed by wall values, so the comparison with data involves no fitted constant.

Figure 4 shows the constant-flux cases at the two ends of the Prandtl-number range together with the asymptote. At $Pr = 0.01$ the conductive layer is thick, ε_θ is nearly uniform across the first viscous units, and the asymptotic regime is fully resolved. The local logarithmic slope of $\mathcal{R}_h$ over $0.4 < y^+ < 2$ is -1.98 to -1.99 at all three Reynolds numbers, the data lie on the analytical amplitude to within 1% at the first grid points, and the $(y^+)^{-2}$ asymptote is followed over more than three decades in $\mathcal{R}_h$. At $Pr = 0.71$ the divergence spans two decades and approaches the same asymptote at the wall, with a data-to-asymptote ratio of 0.93 at the first grid point. The local slope over the first resolved interval is steeper, ≈ -2.6, because ε_θ still varies across the thin conductive layer, so the measured slope contains the finite-y^+ variation of the amplitude factor. This contribution disappears at low Pr. In both cases the exponent -2 is the analytical wall limit, while the wall distance at which it is attained is set by the thickness of the conductive layer.

Figure 5(a) compares the four thermal conditions of Flageul *et al.* [19]. At the Dirichlet wall the ratio is regular and anchored at Pr. At the conjugate, Robin and Neumann walls it is singular, with amplitudes ordered by the wall variance, $\overline{\theta^2}_w = 1.04$, 1.34 and 4.28 respectively, as (27) requires. Each singular member follows its own parameter-free asymptote, shown in figure 5(a) with the amplitudes $\overline{\theta^2}_w/(2\varepsilon_{\theta,h}|_w) = 33.7$, 57.7 and 216.5: the data-to-asymptote ratios at the first grid point are 0.85, 0.95 and 0.93, and the local logarithmic slopes over $0.4 < y^+ < 2$ are -2.12, -2.28 and -2.64, all approaching the analytical exponent -2. The ordering of the finite-y^+ steepening follows the growth of the homogeneous dissipation across the conductive layer, $\varepsilon_{\theta,h}(y^+ = 2)/\varepsilon_{\theta,h}|_w = 2.25$, 2.46 and 2.92 for the conjugate, Robin and Neumann walls, consistent with the mechanism identified in figure 4. The amplitude ordering has a simple physical interpretation. The more temperature fluctuation the wall absorbs, the smaller $\overline{\theta^2}_w$ and the weaker the singularity, with the Neumann wall, which absorbs none, as the extreme case.

Figure 5(b) quantifies this interpolation for the conjugate wall through the thermal activity ratio K, the fluid-to-solid ratio of thermal effusivities. In the sweep of Tiselj and Cizelj [20] at solid thickness $d^+ = 300$, the wall variance falls monotonically over four decades from the ideal-isoflux plateau at $K \gg 1$ towards the isothermal limit as $K \to 0$. The conjugate wall thus moves continuously between the anchored and singular limits of §3, with the singular amplitude set by K and the wall thickness. No variance-budget data are available for the conjugate fields, so this statement is at the level of the amplitude $\overline{\theta^2}_w$ in (27) rather than of the full profiles. The practical implication is nevertheless immediate. For a liquid-sodium–steel system $K = O(0.1\text{–}1)$ [20]. This lies within the transition region, so neither ideal thermal condition represents such a wall, and the amplitude of the near-wall singularity becomes a property of the wall material and thickness rather than of the flow alone.

4.4 Closure-error interpretation of the anchored constant-ratio closure

The near-wall structure of the two ratios admits a direct reading as closure errors. Anchoring both constant-ratio closures, with no adjustable constant, at the shared analytical wall value (23) gives the reconstructions $\varepsilon_\theta^{\text{mod}} = \overline{\theta^2}\,\varepsilon/(2kPr)$ for constant R and $\varepsilon_\theta^{\text{mod}} = \overline{\theta^2}\,\varepsilon_h/(2kPr) + \varepsilon_{\theta,ih}$ for constant $\mathcal{R}_h$, the inhomogeneous part entering exactly because the decomposition closes it in (9). With all other quantities taken from the DNS, the relative errors reduce to the identities $e_R = R(y)/Pr - 1$ and $e_{\mathcal{R}_h} = \big(\mathcal{R}_h(y)/Pr - 1\big)\,(1 - f_\theta)$; figure 6 is therefore a re-expression of figures 2 and 3 in closure-error form, not an independent data set. The factor $1 - f_\theta$, equal to $\frac{1}{2}$ at the wall, results from the exact treatment of $\varepsilon_{\theta,ih}$. The errors are shown for the two databases with the finest near-wall resolution, which store the wall point: the Dirichlet case of Flageul *et al.* [19] at $Pr = 0.71$ and the non-fluctuating case of Tiselj and Cizelj [20] at $Pr = 0.01$. At $Pr = 0.71$ both anchored closures reconstruct ε_θ to within $\pm 12\%$ across the conductive and buffer layers, but the residual error resides in different regions. The constant-R form is exact only at $y = 0$; it under-predicts by up to 6% inside the conductive sublayer, over-predicts by up to 11% in the buffer layer, and its error changes sign at the crossing of §4.2, located by the balance (24). The constant-$\mathcal{R}_h$ form remains within 3% for $y^+ < 3$, and its error, below 11%, is one-signed over $1 < y^+ < 30$. A sign-changing error biases the variance budget in opposite directions on either side of the crossing and cannot be removed by any single constant or by a monotone correction; the one-signed, bounded error of the $\mathcal{R}_h$ form is correctable by a monotone Prandtl-number-dependent function. In buoyant flows, where ε_θ feeds back on the production through the thermal time scale, this qualitative difference matters beyond its magnitude. At $Pr = 0.01$ the constant-R error remains within 9% through the thick conductive sublayer, while beyond it no single anchored constant is adequate: since $\mathcal{R}_h$ rises from Pr to $O(0.2)$ across the thermal layer (figure 2), the reconstruction error exceeds an order of magnitude for both forms.

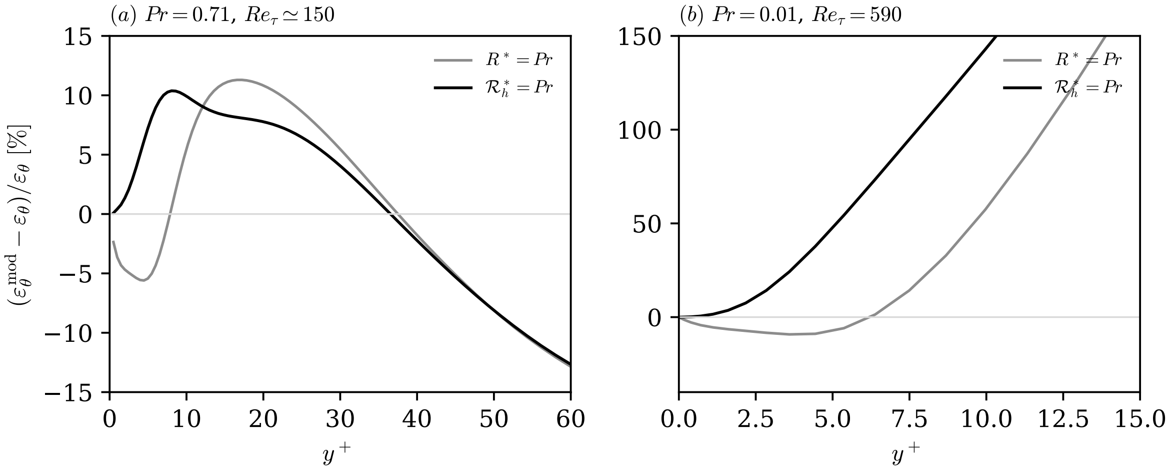

Figure 6: Wall-anchored a priori reconstruction of ε_θ: signed relative error of the constant-R (gray) and constant-$\mathcal{R}_h$ (black) closures, both anchored at the analytical wall value Pr, for (a) the Dirichlet case at $Pr = 0.71$, $Re_\tau \simeq 150$, DNS data [19], and (b) the non-fluctuating case at $Pr = 0.01$, $Re_\tau = 590$, DNS data [20]; both databases store the wall point. The errors equal $R/Pr - 1$ and $(\mathcal{R}_h/Pr - 1)\,(1 - f_\theta)$, respectively; the unweighted comparison of the two ratios is figure 2.

5 Relation to turbulent heat-flux models

The algebraic heat-flux modeling (AHFM) approach has become standard for heat transfer at non-unity Prandtl number in engineering computational fluid dynamics (CFD) practice [32–34]. It follows from the second-moment heat-flux equations under the weak-equilibrium assumption, in which the advection and diffusion of the heat flux are neglected relative to its production and destruction [2, 4, 35], and implicitly assumes local homogeneity. The time-scale ratio consistent with this truncation is therefore the homogeneous ratio $\mathcal{R}_h$ rather than the full R. The equilibrium values of R used in such closures were likewise obtained in a homogeneous framework, in which the transport of $\overline{\theta^2}$ and ε_θ vanishes by construction [3, 36]. Nor is the assumption confined to algebraic models. Any four-equation $(k, \varepsilon, \overline{\theta^2}, \varepsilon_\theta)$ closure [37, 38] embeds it, because the production and destruction terms of the modeled ε_θ equation are formed as coefficients times a mechanical or inverse-mechanical time scale, which is algebraically equivalent to prescribing R. The homogeneous ratio $\mathcal{R}_h$ is the quantity these closures implicitly use. In the following we briefly discuss two challenging engineering cases.

In liquid metals the Reynolds analogy and a constant turbulent Prandtl number are inapplicable, and AHFM closures have been identified as the most promising route across the natural-, mixed- and forced-convection regimes [34], with calibrated variants in engineering use [33]. In the model of Kenjereš *et al.* [32], implemented in the commercial code STAR-CCM+, the ratio is held constant, the leading-order statement $\mathcal{R}_h \simeq$ const. The closure-error interpretation of §4.4 quantifies the consequence: the single constant is adequate for $Pr = O(1)$ and fails by up to an order of magnitude at liquid-metal Prandtl numbers, where the wall value $\mathcal{R}_h|_w = Pr$ is small and the ratio varies across the thermal layer. The departure is large in the microscale variables. Ristorcelli [8] finds the homogeneous ratio bounded, $r_\infty = O(1)$, whereas $\mathcal{R}_h|_w = Pr$ corresponds to $r|_w = 1/Pr \approx 40$–100 for a liquid metal, an order of magnitude outside the homogeneous range and consistent with the known deficiencies of constant-ratio closures at low Pr. Here r denotes, as in Ristorcelli [8], the mechanical-to-thermal time-scale ratio, the inverse $r = 1/R$. Moreover, the walls of liquid-metal systems are conjugate. With $K = O(0.1$–$1)$ for sodium on steel, figure 5(b) places them in the transition region between the anchored and singular limits, so the near-wall treatment must carry the wall variance $\overline{\theta^2}_w$, equivalently K and the wall thickness, as a parameter. The data suggest the functional skeleton of the leading correction: an anchored, monotone interpolation $\mathcal{R}_h(y^+) = Pr + (\mathcal{R}_{h,\infty} - Pr)\, g(y^+)$, with g monotone between $g(0) = 0$ and $g \to 1$ outside the thermal layer and $\mathcal{R}_{h,\infty} = O(0.2)$ at liquid-metal Prandtl numbers (figure 2), supplemented at walls with finite wall variance by the singular amplitude $\overline{\theta^2}_w/(2\varepsilon_{\theta,h}|_w)$ of (27) through the thermal activity ratio. The construction of such a closure, its a posteriori assessment, and an assessment of the analysis in buoyancy-driven configurations such as Rayleigh–Bénard convection are beyond the scope of the present analysis and are left to future work.

The same reasoning applies to supercritical-pressure heat transfer, where the strong property variation through the pseudo-critical region produces large excursions of the local Prandtl number. Constant-ratio AHFM computations reproduce such flows only after one model coefficient is made a function of a non-dimensional property group [39–41]. The present result suggests the molecular Prandtl number, through $\mathcal{R}_h|_w = Pr$ at an isothermal wall, as the physical origin of that dependence. Heated supercritical channels and rods are constant-flux configurations, however, for which (27) makes both ratios singular at the wall, as demonstrated in figure 4. A finite wall anchor is therefore not available. The use of $\mathcal{R}_h$ there rests on its consistency with the AHFM truncation and on its reduced variation outside the wall layer, while the wall itself requires a separate near-wall treatment.

6 Summary

The temperature-variance dissipation rate splits exactly into a homogeneous part $\varepsilon_{\theta,h}$ and a closed inhomogeneous part equal to the molecular diffusion of the variance, defining the homogeneous time-scale ratio $\mathcal{R}_h = \overline{\theta^2}\, \varepsilon_h/(2k\, \varepsilon_{\theta,h})$. Through the mechanical and thermal Taylor microscales the ratio takes the form $\mathcal{R}_h = (5/C_\theta)Pr(\lambda_\theta/\lambda)^2$, from which the near-wall behavior follows analytically: at an isothermal wall both microscales are linear in the wall distance, $\mathcal{R}_h$ is smooth and $\mathcal{R}_h|_w = Pr$, whereas at a constant-flux wall the thermal microscale stays finite and the ratio diverges as $\overline{\theta^2}_w\, (y^+)^{-2}$ with an amplitude fixed by wall values. Channel-flow DNS from three independent codes confirm the wall limit at $Pr = 0.71$, 0.025 and 0.01, the monotone anchored approach of $\mathcal{R}_h$ in contrast to the departure-and-return of R, the singular asymptote with its analytical amplitude, and the interpolation of the conjugate wall between the two limits through the thermal activity ratio. The classical and homogeneous ratios are related by the exact factorization $R = \mathcal{R}_h(1-f_\theta)/(1-f_u)$ of (17), an immediate consequence of the definitions introduced to explain the near-wall crossing of R: the inhomogeneous fractions $f_\theta = \varepsilon_{\theta,ih}/\varepsilon_\theta$ and $f_u = \varepsilon_{ih}/\varepsilon$ carry the entire difference between the two ratios, equal one half at an isothermal wall, and reduce the departure and return of R to the balance (24) between the departure of $\mathcal{R}_h$ from its anchor and the imbalance of the fractions. Because the mechanical fraction is a property of the velocity field alone, the crossing of R through its wall value is tied to the sign change of ε_{ih} at the inflection point of k and scales in viscous units, at $y^+ \approx 6$–8 in all ten isothermal cases; the same fractions organize the wall-anchored closure errors, $e_R = R/Pr - 1$ and $e_{\mathcal{R}_h} = (\mathcal{R}_h/Pr - 1)(1 - f_\theta)$, the latter one-signed near the wall. The construction provides a physical basis for the constant time-scale ratio commonly used in turbulent heat-flux models, together with the leading, Prandtl-number-dependent correction relevant to low-Prandtl and supercritical fluids.

Exact analytical results of this kind are increasingly used to inform data-driven turbulence closures. Physics-informed and machine-learning approaches for the Reynolds stresses and scalar transport have developed rapidly [e.g. 42, 43]. Ling *et al.* [44] construct a physically more consistent model by integrating the analytical result on the Galilean, rotational and reflectional invariance of turbulence models by Pope [45] into the machine-learning process. A perspective on the present analytical results, employed as constraints within a physics-informed neural network for homogeneous isotropic turbulence, is given in our recent work [46]. The constraint is the pair formed by the exact identity (12) and the analytical near-wall results, which together restrict the modeled scalar dissipation in the same way the invariance results of Pope [45] restrict the modeled stresses.

Acknowledgments

This study was supported by Technological Research Council of Türkiye (TÜBİTAK), Project No. 123M535, and by the European Union co-funded partnership CONNECT-NM under Grant Agreement No. 101165375. The channel-flow data of Abe, Kawamura and co-workers were obtained from the JAXA DNS database; the data of Flageul and co-workers from the public repository of the Jožef Stefan Institute; and the $Pr = 0.01$ database was kindly provided by I. Tiselj. The author reports no conflict of interest.

Data availability

The DNS databases analyzed here are available from the JAXA DNS database [18], from the repository `repo.ijs.si/CFLAG/incompact3d` [19], and from the authors of Tiselj and Cizelj [20]. The processing scripts and derived profiles are available from the author on reasonable request.

References

[1] S. Corrsin, J. Aeronaut. Sci. **18**, 417 (1951).

[2] B. E. Launder, Trans. ASME J. Heat Transfer **110**, 1112 (1988).

[3] G. R. Newman, B. E. Launder, and J. L. Lumley, J. Fluid Mech. **111**, 217 (1981).

[4] K. Hanjalić, Annu. Rev. Fluid Mech. **34**, 321 (2002).

[5] J. L. Lumley and G. R. Newman, J. Fluid Mech. **82**, 161 (1977).

[6] Z. Warhaft and J. L. Lumley, J. Fluid Mech. **88**, 659 (1978).

[7] Z. Warhaft, Annu. Rev. Fluid Mech. **32**, 203 (2000).

[8] J. R. Ristorcelli, Phys. Fluids **18**, 075101 (2006).

[9] M. R. Overholt and S. B. Pope, Phys. Fluids **8**, 3128 (1996).

[10] S. C. Lin and S. C. Lin, Phys. Fluids **16**, 1587 (1973).

[11] I. Otić, G. Grötzbach, and M. Wörner, J. Fluid Mech. **525**, 237 (2005).

[12] B. A. Kolovandin and I. A. Vatutin, Int. J. Heat Mass Transfer **15**, 2371 (1972).

[13] J. Jovanović, Q.-Y. Ye, and F. Durst, J. Fluid Mech. **293**, 321 (1995).

[14] P. Y. Chou, Quart. Appl. Math. **3**, 38 (1945).

[15] J. M. Burgers, in *Proc. K. Ned. Akad. Wet., Ser. B*, Vol. 6 (1953) pp. 125–147.

[16] S. Jakirlić and K. Hanjalić, J. Fluid Mech. **459**, 139 (2002).

[17] S. Jakirlić and J. Jovanović, J. Fluid Mech. **656**, 530 (2010).

[18] H. Abe, R. A. Antonia, and H. Kawamura, J. Fluid Mech. **627**, 1 (2009).

[19] C. Flageul, S. Benhamadouche, É. Lamballais, and D. Laurence, Int. J. Heat Fluid Flow **55**, 34 (2015).

[20] I. Tiselj and L. Cizelj, Nucl. Eng. Des. **253**, 153 (2012).

[21] J. W. Deardorff, in *Proceedings of the Workshop on Micrometeorology*, Vol. 271 (American Meteorological Society, Boston, MA, 1973) pp. 271–311.

[22] K. Hanjalić and B. E. Launder, Journal of Fluid Mechanics **52**, 609 (1972).

[23] J. O. Hinze, *Turbulence*, 2nd ed. (McGraw-Hill, 1975).

[24] M. Kholmyansky and A. Tsinober, Phys. Fluids **20**, 041704 (2008).

[25] M. Kholmyansky, V. Sabelnikov, and A. Tsinober, in *Turbulence and Interactions*, edited by M. Deville, T.-H. Lê, and P. Sagaut (Springer, 2010) pp. 215–221.

[26] G. I. Taylor, Proc. R. Soc. Lond. A **151**, 421 (1935).

[27] H. Tennekes and J. L. Lumley, *A First Course in Turbulence* (MIT Press, 1972).

[28] C. Flageul, S. Benhamadouche, É. Lamballais, and D. Laurence, Int. J. Heat Mass Transfer **111**, 321 (2017).

[29] H. Kawamura, H. Abe, and Y. Matsuo, Int. J. Heat Fluid Flow **20**, 196 (1999).

[30] H. Abe, H. Kawamura, and Y. Matsuo, Int. J. Heat Fluid Flow **25**, 404 (2004).

[31] N. Kasagi, Y. Tomita, and A. Kuroda, Trans. ASME J. Heat Transfer **114**, 598 (1992).

[32] S. Kenjereš, S. B. Gunarjo, and K. Hanjalić, Int. J. Heat Fluid Flow **26**, 569 (2005).

[33] A. Shams, F. Roelofs, E. Baglietto, S. Lardeau, and S. Kenjereš, Int. J. Heat Mass Transfer **79**, 589 (2014).

[34] F. Roelofs, A. Shams, I. Otić, M. Böttcher, M. Duponcheel, Y. Bartosiewicz, D. Lakehal, E. Baglietto, S. Lardeau, and X. Cheng, Nucl. Eng. Des. **290**, 99 (2015).

[35] B. J. Daly and F. H. Harlow, Phys. Fluids **13**, 2634 (1970).

[36] S. E. Elghobashi and B. E. Launder, Phys. Fluids **26**, 2415 (1983).

[37] Y. Nagano and C. Kim, Trans. ASME J. Heat Transfer **110**, 583 (1988).

[38] S. Manservisi and F. Menghini, Int. J. Heat Mass Transfer **69**, 312 (2014).

[39] A. Pucciarelli and W. Ambrosini, Ann. Nucl. Energy **99**, 58 (2017).

[40] A. Pucciarelli and W. Ambrosini, Int. J. Heat Mass Transfer **127**, 1138 (2018).

[41] A. Alasif, A. Pucciarelli, and A. Shams, Prog. Nucl. Energy **193**, 106190 (2026).

[42] J.-X. Wang, J.-L. Wu, and H. Xiao, Phys. Rev. Fluids **2**, 034603 (2017).

[43] J.-L. Wu, H. Xiao, and E. Paterson, Phys. Rev. Fluids **3**, 074602 (2018).

[44] J. Ling, A. Kurzawski, and J. Templeton, J. Fluid Mech. **807**, 155 (2016).

[45] S. B. Pope, J. Fluid Mech. **72**, 331 (1975).

[46] D. Günseren, O. Ertunç, I. Ari, A. A. Atik, N. Muhtaroglu, and I. Otić, J. Comput. Phys. **553**, 114725 (2026).